

Urban GNSS Positioning for Consumer Electronics: 3D Mapping and Advanced Signal Processing

Jiale Wang, *Member, IEEE*, Ming Xia, Deyou Zhang, *Member, IEEE*, Weisong Wen, Wu Chen, Chuang Shi

Abstract—Smartphones, as ubiquitous consumer electronics devices, rely heavily on Global Navigation Satellite Systems (GNSS) for various applications, including navigation and location-based services. However, the small-sized and low-cost patch antennas used in smartphones are particularly susceptible to multipath effects and signal degradation, posing significant challenges for accurate positioning in urban environments. To address these issues, this study introduces a 3D-mapping-aided Precise Point Positioning (3DMA PPP) algorithm. The algorithm incorporates 3D building models to exclude non-line-of-sight (NLOS) satellites, while mitigating potential multipath effects and thermal noise on line-of-sight (LOS) satellites using Doppler smoothing filters and an optimized carrier-to-noise ratio (C/N_0)-dependent stochastic model. Experiments conducted with Xiaomi Mi8 and Huawei Mate40 smartphones demonstrate that the proposed method achieves positioning errors within 2 m, while improving the positioning accuracy of low-cost GNSS receivers to sub-meter levels. The results show a more than 50% improvement in positioning accuracy compared to conventional algorithms, significantly enhancing the utility of consumer-grade devices for urban navigation. This work highlights the potential for advanced GNSS techniques to empower consumer electronics with precise and reliable positioning capabilities.

Index Terms—Consumer electronics, GNSS, smartphones, 3D building models, accurate positioning, urban navigation, stochastic modeling, signal processing.

I. INTRODUCTION

THE active number of Internet of Things (IoT) devices, including smartphones, wearables, and unmanned aerial vehicles (UAVs), is expected to exceed 75 billion by 2025 [1]. Modern consumer electronics are increasingly powerful, equipped with faster and smaller processor chipsets than the mainframe computers of decades ago. With the popularization of wearable devices and smartphones, GNSS positioning services will be extended to a wide range of fields, such as intelligent transportation [2], smart industry [3] and smart cities [4].

Application scenarios, such as lane-level navigation and sidewalk-level positioning, require smartphones to provide high-precision positioning information [5], [6]. Therefore, the accuracy of standard point positioning (SPP), which is typically

5–10 m, can no longer meet the growing needs of users. Fortunately, smartphones equipped with the Google Android operating system have been able to obtain raw GNSS observations through application programming interfaces (APIs) since May 2016, which has inspired researchers to develop more techniques to improve positioning capabilities [7].

However, the adoption of low-cost GNSS chipsets and small-sized patch antennas has led to a noticeable degradation in the quality of smartphone GNSS observations, with a significant increase in thermal noise and multipath errors in raw GNSS measurements [8]. Additionally, due to the obstruction and reflection of satellite signals by tall buildings in urban environments, smartphone GNSS measurements inevitably suffer from substantial ranging errors, especially in NLOS reception. To mitigate the impact of these factors on smartphone-based GNSS positioning, this study introduces a 3D-mapping-aided precise point positioning algorithm. Static and kinematic vehicle experiments were carried out in typical urban areas with 3D building models, and the performance of the proposed algorithm on low-cost smartphones and receivers was evaluated and discussed in detail.

The contributions of this study are as follows:

- 1) A dual-frequency and multi-GNSS PPP model tailored for low-cost smart devices has been established. This model accounts for the inconsistencies in dual-frequency measurements of smartphones and aims to fully exploit the positioning capabilities by integrating raw GNSS measurements from multiple constellations.
- 2) A two-step rapid NLOS satellite detection method is proposed. Initial approximate position is swiftly achieved through SPP processing of high-elevation satellites, followed by the generation of a sky mask via mapping matching with 3D models to classify NLOS and LOS satellites. This method ensures the effective exclusion of NLOS multipath in PPP processing, safeguarding against positioning degradation.
- 3) A Doppler smoothing filter (DSF) algorithm and an optimized Carrier-to-Noise Ratio (C/N_0)-dependent stochastic model suitable for low-cost smart devices have

This work was supported by the National Key Research and Development Program of China under Grant 2022YFB3904604. (Corresponding author: Ming Xia, Deyou Zhang).

Jiale Wang, Ming Xia, Deyou Zhang and Chuang Shi are with the School of Electronics and Information Engineering, Beihang University, Beijing 100091, China (e-mail: wangjiale@buaa.edu.cn; xiaming@buaa.edu.cn; deyou@buaa.edu.cn; shichuang@buaa.edu.cn).

Weisong Wen is with the Department of Aeronautical and Aviation Engineering, Hong Kong Polytechnic University, Hong Kong (e-mail: welson.wen@polyu.edu.hk).

Wu Chen is with the Department of Land Surveying and Geo-Information at Hongkong Polytechnic University, Hongkong, China (e-mail: wu.chen@polyu.edu.hk).

been proposed. This algorithm can suppress over 73% of LOS multipath errors, thereby enhancing the estimation accuracy of the PPP model.

- 4) To support the rapidly evolving consumer electronics landscape, the BUAA RINEX Convertor software has been developed and open-sourced at <https://github.com/Jia-le-wang/BUAA-RINEX-Convertor>. This tool addresses RINEX conversion errors found in existing software and ensures compatibility with advanced GNSS features.

The remainder of this paper is organized as follows. Section II reviews related work on high-precision GNSS positioning of smartphones. Section III describes the proposed algorithm and its architecture. Section IV details the experimental design and analysis of the results. Finally, Section V summarizes the study, draws conclusions, and discusses future research.

II. RELATED WORK

This section reviews research on the detection and mitigation strategies of NLOS and LOS multipaths, as well as their shortcomings. Section II-A introduces state-of-the-art NLOS satellite detection methods, while Section II-B describes the advanced LOS multipath error mitigation strategies.

A. State-of-the-art NLOS Multipath Detection Methods

In an urban environment, where most smartphones use location services, the NLOS reception caused by buildings' occlusion and reflection is unavoidable and will significantly deteriorate positioning performance. To detect and exclude NLOS satellites in urban areas efficiently, Groves and Adjrad [9] proposed a famous 3D-mapping-aided (3DMA) GNSS technique. They used a Leica, u-blox, and Nexus tablet to verify the algorithm in the London area with 3D models, achieving horizontal position errors (Root Mean Square, RMS) of 3.5 m, 4.7 m, and 4.9 m, respectively. Ng et al. [10] integrated dual-frequency smartphone measurements from the L5 band into the 3DMA GNSS framework to enhance positioning performance in urban areas. Experiments demonstrated that positioning solutions derived from L1-L5 3DMA GNSS were superior to those from 3DMA GNSS using only the L1 band, with an average positioning accuracy within 10 meters. However, these studies predominantly utilize standard point positioning (SPP) based on GNSS pseudorange measurements in their positioning processes, resulting in positioning accuracy for smartphones that remains at several meters or even worse, which is insufficient to meet the high-precision positioning requirements of vehicles.

Other scholars have considered the use of additional sensors and technical methods for NLOS multipath detection. Wen et al. [11] adopted a sky-pointing fisheye camera to assist in the identification of NLOS satellites and performed different weighting processes on the observation of NLOS and LOS signals, thus effectively reducing the occurrence of GNSS outliers. Subsequently, they attempted to use 3D LiDAR for the detection, reshaping, and even correction of NLOS multipath [12], [13]. However, these technical methods are difficult to apply

directly to integrated, low-cost smartphones due to the expensive sensor costs and the stringent usage conditions requiring vertical orientation towards the sky.

B. Advanced LOS Multipath Error Mitigation Strategies

The methods mentioned above can effectively detect and eliminate NLOS signals, with the retained LOS signals being used to perform positioning processing. However, due to the limitations of the small linearly polarized patch antennas embedded in smartphones, the measured LOS signals still suffer from severe multipath interference and thermal noise. Benvenuto et al. [14] used the Hatch filter algorithm to compensate for LOS multipath errors in a static environment and verified the effectiveness of this method based on the Xiaomi Mi8 smartphone. However, the Hatch filter is prone to gradual divergence due to the influence of carrier phase cycle slips and accumulated ionospheric errors. Especially in complex urban environments, the carrier phase measurements of smartphones are frequently interrupted, and they suffer from cycle slips due to obstructions by buildings, which can lead to rapid deterioration of the filter's performance. Zhou et al. [15] developed a Doppler-smoothed code method based on the principle of minimum variance, taking advantage of the powerful Doppler observation function and not being affected by cycle slips, demonstrating significant advantages in urban environments.

In addition, some scholars consider suppressing LOS multipath error from the perspective of the stochastic model. Ng et al. [16] adopted an improved weighting model based on carrier-to-noise ratio and elevation, assigning appropriate weights between measurements at the L1 and L5 bands, achieving a root mean square error of less than 10 m in most urban scenarios. Shinghal and Bisnath [17] confirmed the correlation between satellite elevation, carrier-to-noise ratio, and multipath for smartphone GNSS, showing that smartphone GNSS multipath is only correlated with carrier-to-noise ratio. An empirical carrier-to-noise ratio-dependent stochastic model could improve the positioning accuracy of smart devices. Unfortunately, these studies have not yet considered the variability in GNSS measurement accuracy across different types of smart devices, multiple satellite systems, and multiple frequencies, therefore cannot fully exploit the positioning potential.

III. MATERIALS AND METHODS

This section describes the architecture and implementation of the proposed algorithm. Fig. 1 shows the overall architecture of the algorithm proposed in this study, including the generation of a 3D building models database, raw GNSS observation conversion, International GNSS Service (IGS) correction reception, error correction models, GNSS preprocessing, SPP processing, and PPP processing. Section III-A introduces the dual-frequency and multi-GNSS PPP model. Section III-B details the 3D-mapping-aided NLOS satellite detection algorithm. Section III-C derives the equations for the Doppler smoothing filter, while Section III-D obtains the optimized C/N₀-dependent stochastic model through correlation analysis and residual fitting.

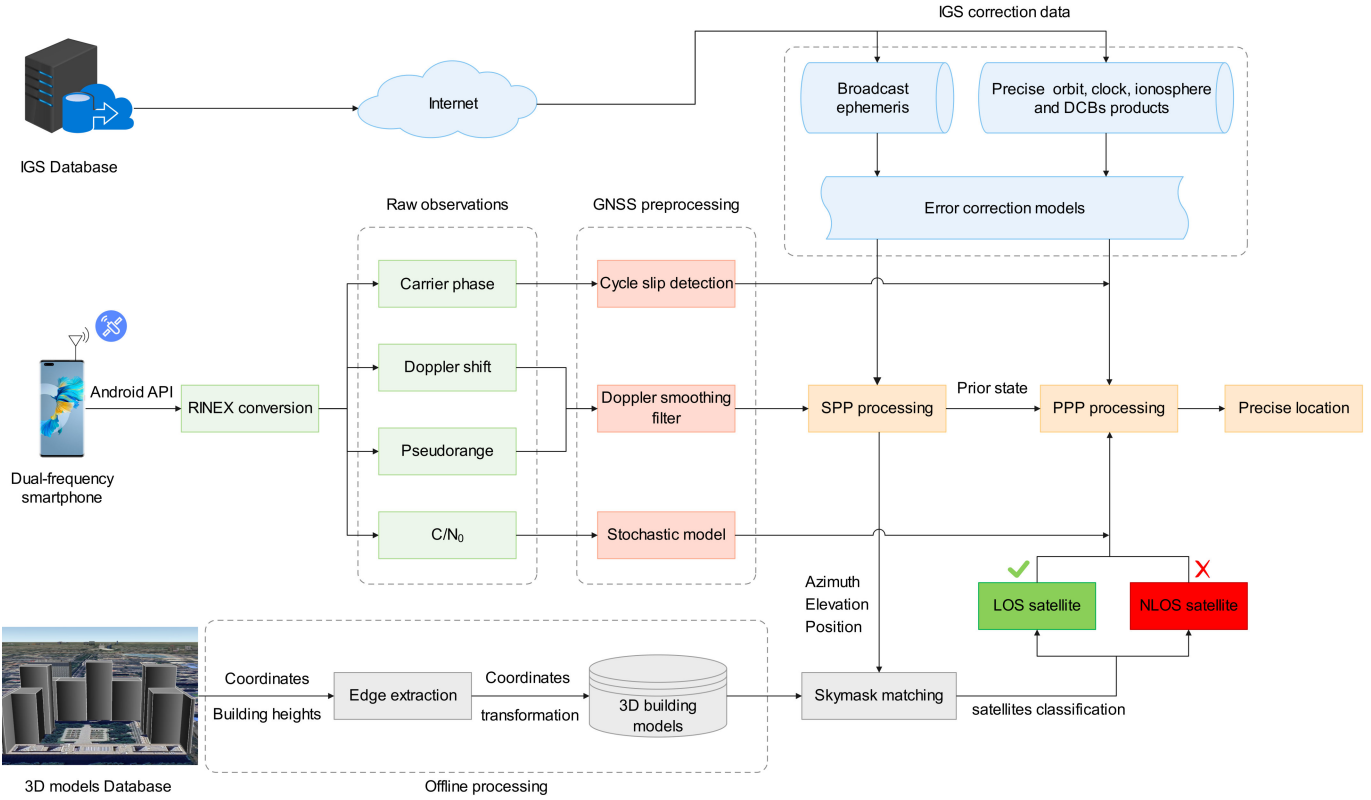


Fig. 1. Overall architecture of 3D-mapping-aided precise point positioning algorithm for low-cost smartphones.

A. Dual-frequency and Multi-GNSS PPP model

Precise point positioning (PPP) is a technical means of correcting each error in the GNSS propagation path using precise satellite orbits, clocks, ionosphere, and differential code biases (DCBs). Because the dual-frequency GPS signals measured by smartphones are in the L1 and L5 bands, there are only 16 satellites that support L5 signals (the number of satellites broadcasting L1 signals is 32), which makes the dual-frequency signals (L1+L5) measured simultaneously insufficient. If the dual-frequency ionosphere-free PPP model commonly used in most research is adopted, L1 signals tracked on satellites that cannot capture the L5 signal will be discarded. Moreover, the ionosphere-free PPP model significantly amplifies observation noise, which poses an even greater disaster for low-cost smartphones.

To take full advantage of raw multi-GNSS observations from smartphones, an undifferenced and uncombined PPP model was considered in this study. The basic observation model for undifferenced and uncombined PPP is as follows:

$$\begin{cases} P_{r,f}^{K,s} = \rho_r^{K,s} + c \cdot (t_r^K - t^{K,s}) + \mu_r^{K,s} \cdot T_r + \gamma_{r,f}^{K,s} \cdot I_r^{K,s} \\ \quad + c \cdot (b_{r,f}^K - b_f^{K,s}) + \varepsilon_{pK} \\ \phi_{r,f}^{k,s} = \rho_r^{k,s} + c \cdot (t_r^K - t^{K,s}) + \mu_r^{K,s} \cdot T_r - \gamma_{r,f}^{K,s} \cdot I_r^{K,s} \\ \quad - \lambda_f^K \cdot (N_{r,f}^{K,s} + B_{r,f}^K - B_f^{K,s}) + \varepsilon_{\phi K} \end{cases} \quad (1)$$

where subscript *f* and *r* are the abbreviations of signal frequency and receiver, respectively; superscript *K* and *s* represent the satellite system and space vehicle number (SVN), respectively; *K* specifically stands for a satellite system in GPS, GLONASS, BDS, GALILEO and QZSS, and its abbreviations correspond to G, R, C, E and J, respectively; $\phi_{r,f}^{k,s}$ and $P_{r,f}^{K,s}$ denote the carrier phase and code pseudorange observations in meters, respectively; $\rho_r^{K,s}$ represents the geometric distance between the receiver and the satellite; *c* is the speed of light in vacuum; t_r^K and $t^{K,s}$ are receiver clock error and satellite clock error, respectively; T_r and $\mu_r^{K,s}$ represent the zenith tropospheric delay and the corresponding mapping function, respectively; $I_r^{K,s}$ and $\gamma_{r,f}^{K,s}$ represent the zenith ionospheric delay and the projection function, respectively; λ_f^K and $N_{r,f}^{K,s}$ represent the wavelength and integer ambiguity of the carrier phase, respectively; $b_{r,f}^K$ and $b_f^{K,s}$ represent the receiver-related and satellite-related code hardware delay, respectively; $B_{r,f}^K$ and $B_f^{K,s}$ denote receiver-related and satellite-related phase hardware delay, respectively; ε_{pK} and $\varepsilon_{\phi K}$ are the observation noise of code pseudorange and carrier phase, respectively.

For ionospheric and tropospheric delays, the global ionospheric maps (GIM) and global pressure and temperature 2 wet (GPT2w) model are usually used as prior information for error correction in PPP processing [18], [19]. However, the precise

clock products provided by the IGS Analysis Center are generated based on a dual-frequency (L1+L2) ionosphere-free combination that absorbs its hardware delay. Therefore, we need to convert the clock error of the L1+L5 frequencies measured by the smartphone to match IGS products [20], [21]. The DCBs between two signals can usually be expressed as:

$$DCB_{mn}^{K,S} = b_m^{K,S} - b_n^{K,S} \quad (2)$$

where m and n represent the frequencies of two different signals, respectively ($m, n = 1, 2, 5; m \neq n$); $DCB_{mn}^{K,S}$ represents the differential code bias between two signals. Assuming that the precise clock error provided by the IGS is $t_{IGS}^{K,S}$, the real satellite clock error $t^{K,S}$ can be expressed as:

$$t_{IGS}^{K,S} = t^{K,S} + \alpha_{mn}^K \cdot b_m^{K,S} + \beta_{mn}^K \cdot b_n^{K,S} \quad (3)$$

where α_{mn}^K and β_{mn}^K are the coefficients of the code hardware delay, respectively, and their specific forms can be expressed as:

$$\alpha_{mn}^K = \frac{(f_m^K)^2}{(f_m^K)^2 - (f_n^K)^2}, \beta_{mn}^K = -\frac{(f_n^K)^2}{(f_m^K)^2 - (f_n^K)^2} \quad (4)$$

In addition, we use a float solution to estimate the integer

$$\begin{cases} P_{r,1}^{K,S} = \rho_r^{K,S} + c \cdot (t_r^K - t_{IGS}^{K,S} + \beta_{12}^K \cdot DCB_{12}^{K,S}) + \mu_r^{K,S} \cdot T_r + \gamma_{r,1}^{K,S} \cdot I_r^{K,S} + \varepsilon_{P_{r,1}^K} \\ P_{r,5}^{K,S} = \rho_r^{K,S} + c \cdot (t_r^K + b_r^K - t_{IGS}^{K,S} - DCB_{15}^{K,S} + \beta_{12}^K \cdot DCB_{12}^{K,S}) + \mu_r^{K,S} \cdot T_r + \gamma_{r,5}^{K,S} \cdot I_r^{K,S} + \varepsilon_{P_{r,5}^K} \\ \phi_{r,1}^{K,S} = \rho_r^{K,S} + c \cdot (t_r^K - t_{IGS}^{K,S}) + \mu_r^{K,S} \cdot T_r - \gamma_{r,1}^{K,S} \cdot I_r^{K,S} + \lambda_1^K \cdot \tilde{N}_{r,1}^{K,S} + \varepsilon_{\phi_{r,1}^K} \\ \phi_{r,5}^{K,S} = \rho_r^{K,S} + c \cdot (t_r^K - t_{IGS}^{K,S}) + \mu_r^{K,S} \cdot T_r - \gamma_{r,5}^{K,S} \cdot I_r^{K,S} + \lambda_5^K \cdot \tilde{N}_{r,5}^{K,S} + \varepsilon_{\phi_{r,5}^K} \end{cases} \quad (6)$$

where $DCB_{12}^{K,S}$ and $DCB_{15}^{K,S}$ can be provided and corrected through the IGS database; $P_{r,1}^{K,S}$ and $\phi_{r,1}^{K,S}$ are code pseudorange and carrier phase in meters at L1 frequency; $P_{r,5}^{K,S}$ and $\phi_{r,5}^{K,S}$ are code pseudorange and carrier phase in meters at L5 frequency; $\varepsilon_{P_{r,1}^K}$ and $\varepsilon_{P_{r,5}^K}$ are the pseudorange observation noise at L1 and L5 frequencies, respectively; and $\varepsilon_{\phi_{r,1}^K}$ and $\varepsilon_{\phi_{r,5}^K}$ are the carrier phase observation noise at L1 and L5 frequencies, respectively.

Assuming that a dual-frequency smartphone tracks j satellites in a given epoch, the corresponding observation model in the matrix form of (6) can be expressed as:

$$\mathbf{V} = \mathbf{A} \cdot \mathbf{X} - \mathbf{L}, \mathbf{P} \quad (7)$$

The specific form of the weighting matrix \mathbf{P} is provided in detail in Section III-D. \mathbf{V} , \mathbf{X} , \mathbf{A} and \mathbf{L} represent the residual matrix, the parameter matrix to be estimated, the design matrix and the observation matrix, respectively. For the sake of brevity and clarity, their specific form is expressed as:

ambiguity of the carrier phase, therefore, it can be considered that the phase hardware delay is completely absorbed by the ambiguity [22]:

$$\tilde{N}_{r,f}^{K,S} = N_{r,f}^{K,S} + B_{r,f}^K - B_f^{K,S} \quad (5)$$

where $\tilde{N}_{r,f}^{K,S}$ represents the ambiguity that absorbs the phase hardware delay. It is generally observed that for survey-grade receivers, the delay consistency between different frequency signals of each constellation is well-maintained, with receiver clock offsets absorbing code hardware delays without separate estimation. For low-cost smartphones, significant discrepancies can arise between L1 and L5 frequency clock offsets due to the inherent inconsistencies in code hardware delays. Neglecting these inter-frequency delays could adversely affect positioning accuracy. Nevertheless, introducing two new parameters to be estimated will cause the matrix formed by the observation equation to be rank deficient. Because the code hardware delays $b_{r,f}^K$ of the signals on different channels of the receiver are linearly related, we set $b_{r,1}^K = 0$ to obtain a unique solution b_r^K at the L5 frequency [23].

Therefore, the PPP observation equation with dual-frequency (L1+L5) observations, including IGS precise clocks and DCBs corrections, can be expressed as:

$$\begin{cases} \mathbf{V} = (\mathbf{V}_{P_{r,1}^K} \ \mathbf{V}_{P_{r,5}^K} \ \mathbf{V}_{\phi_{r,1}^K} \ \mathbf{V}_{\phi_{r,5}^K})^T \\ \mathbf{A} = (\mathbf{A}_{\Delta r_r} \ \mathbf{A}_{t_r^K} \ \mathbf{A}_{b_r^K} \ \mathbf{A}_{\tilde{N}_{r,1}^{K,S}} \ \mathbf{A}_{\tilde{N}_{r,5}^{K,S}} \ \mathbf{A}_{\Delta I_r^K} \ \mathbf{A}_{\Delta T_w^K})^T \\ \mathbf{X} = (\Delta \mathbf{r}_r \ \mathbf{t}_r^K \ \mathbf{b}_r^K \ \tilde{\mathbf{N}}_{r,1}^{K,S} \ \tilde{\mathbf{N}}_{r,5}^{K,S} \ \Delta \mathbf{I}_r^K \ \Delta \mathbf{T}_w) \\ \mathbf{L} = (\Delta \mathbf{P}_{r,1}^K \ \Delta \mathbf{P}_{r,5}^K \ \Delta \boldsymbol{\phi}_{r,1}^K \ \Delta \boldsymbol{\phi}_{r,5}^K) \end{cases} \quad (8)$$

where $\Delta \mathbf{P}_{r,1}^K = (\Delta P_{r,1}^{K,1} \dots \Delta P_{r,1}^{K,j})^T$ and $\Delta \boldsymbol{\phi}_{r,1}^K = (\Delta \phi_{r,1}^{K,1} \dots \Delta \phi_{r,1}^{K,j})^T$ are observed-minus-computed (OMC) of code pseudorange and carrier phase of L1 frequency, respectively; $\Delta \mathbf{P}_{r,5}^K = (\Delta P_{r,5}^{K,1} \dots \Delta P_{r,5}^{K,j})^T$ and $\Delta \boldsymbol{\phi}_{r,5}^K = (\Delta \phi_{r,5}^{K,1} \dots \Delta \phi_{r,5}^{K,j})^T$ are observed-minus-computed (OMC) of code pseudorange and carrier phase of L5 frequency, respectively; $\Delta \mathbf{r}_r = (\Delta x_r \ \Delta y_r \ \Delta z_r)^T$ is the three-dimensional component of the estimated receiver coordinates; \mathbf{t}_r^K and \mathbf{b}_r^K denote the estimated receiver clock error of each satellite system and the code hardware delay on the second frequency, respectively; $\tilde{\mathbf{N}}_{r,1}^{K,S} = (\tilde{N}_{r,1}^{K,1} \dots \tilde{N}_{r,1}^{K,j})^T$ and $\tilde{\mathbf{N}}_{r,5}^{K,S} = (\tilde{N}_{r,5}^{K,1} \dots \tilde{N}_{r,5}^{K,j})^T$ are the ambiguity estimates of the float solution on the L1 frequency and L5 frequency of each satellite, respectively; $\Delta \mathbf{I}_r^K =$

$(I_r^{K,1} \dots I_r^{K,j})^T$ is the residual estimates of zenith ionospheric delay for each satellite, respectively; ΔT_w is the residual estimates of zenith tropospheric delay; $\mathbf{V}_{P_{r,1}^K}$, $\mathbf{V}_{P_{r,5}^K}$, $\mathbf{V}_{\phi_{r,1}^K}$ and $\mathbf{V}_{\phi_{r,5}^K}$ are residual matrix of pseudorange and carrier phase at L1 and L5 frequencies, respectively, and each component in the matrices \mathbf{A} corresponds to the coefficient vector of each parameter to be estimated.

B. 3D-Mapping-Aided NLOS satellite Detection Algorithm

In recent years, 3D maps have gradually replaced abstract 2D map symbols with intuitive 3D terrains and features. This transition has led to the development of dynamic, multi-dimensional, and interactive map modes. As maps become more accurate and the types of available data increase, 3D maps have become auxiliary tools for navigation and positioning. Additionally, by utilizing sky masks generated by 3D building models, it is possible to predict satellite visibility and effectively detect and exclude NLOS signals. Fig. 2 shows a schematic diagram of NLOS/LOS satellite and signal propagation paths due to building obstruction and reflection.

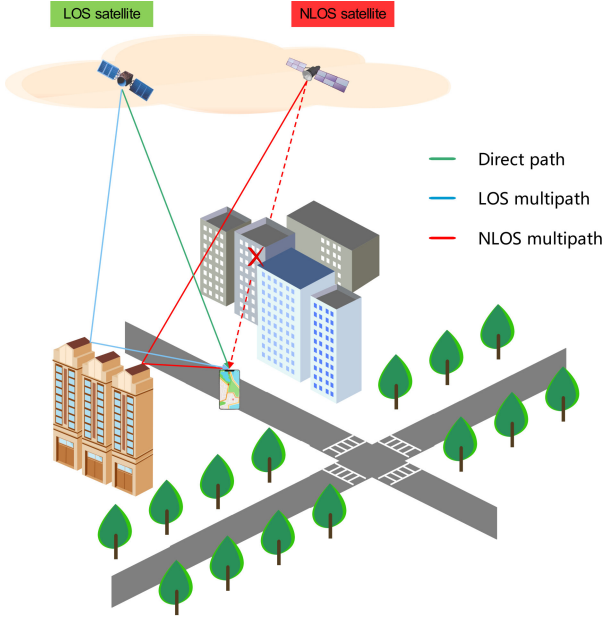


Fig. 2. Schematic diagram of NLOS/LOS satellite and signal propagation paths due to building obstruction and reflection.

For urban areas with 3D building models, ray tracing and building heights can be used to divide blocked and unblocked areas from the perspective of the current test location. As shown in the offline processing stage in Fig. 1, we first need to extract the edge information of buildings based on the 3D map and then generate the sky mask database. Suppose that the coordinates of the i th edge point of the 3D building are (X_i, Y_i, Z_i) and the approximate coordinates obtained by SPP processing are (X_0, Y_0, Z_0) , where all the coordinates are given in the Earth-

centered Earth-fixed (ECEF) coordinate system. We first convert the ECEF coordinates into geodetic coordinates:

$$\begin{cases} \varphi = \arctan \left[\frac{Z_i}{\sqrt{X_i^2 + Y_i^2}} \cdot \left(1 - e^2 \frac{N}{N+h} \right)^{-1} \right] \\ \lambda = \arctan \left(\frac{X_i}{Y_i} \right) \\ h = \frac{\sqrt{X_i^2 + Y_i^2}}{\cos \varphi} - N \end{cases} \quad (9)$$

where $N = \frac{a}{\sqrt{1-e^2 \sin^2 \varphi}}$ and $e^2 = f \cdot (2-f)$; $a = 6378137.0$ m is the semi-major axis of the Earth, and $f = 1/298.25$ is the Earth flattening. After the conversion of (9), the coordinate $(\varphi_0, \lambda_0, h_0)$ of the smartphone in the geodetic coordinate system can be obtained.

In addition, to facilitate the generation of sky masks, it is necessary to convert the ECEF coordinates to local east-north-up (ENU) coordinates centered on the location of the smartphone [24]. The conversion of two coordinate systems can be expressed as follows:

$$\begin{bmatrix} x_i \\ y_i \\ z_i \end{bmatrix} = \begin{bmatrix} -\sin \varphi_0 & \cos \varphi_0 & 0 \\ -\sin \lambda_0 \cos \varphi_0 & -\sin \lambda_0 \sin \varphi_0 & \cos \varphi_0 \\ \cos \lambda_0 \cos \varphi_0 & \cos \lambda_0 \sin \varphi_0 & \sin \varphi_0 \end{bmatrix} \begin{bmatrix} X_i - X_0 \\ Y_i - Y_0 \\ Z_i - Z_0 \end{bmatrix} \quad (10)$$

where (x_i, y_i, z_i) are the edge coordinates of the buildings after coordinate conversion. Therefore, by scanning all azimuths (0-360°) and elevations (0-90°) at the approximate locations of the smartphone, 3D building models can be mapped in the polar coordinate system to generate a satellite sky mask.

Traditionally, 3DMA GNSS methodologies predominantly necessitate the construction of a grid over the area of interest and the calculation of candidate scores at each grid point [25]. For instance, deploying a 1*1 m grid within a 50*50 m urban area would require at least 2500 iterations to identify viable candidate positions using previous approaches. While this method is effective for offline processing, it is challenging to apply in practice for low-cost devices constrained by battery life and processing capacity. In contrast, our algorithm employs a two-step procedure tailored for efficient real-time smartphone localization, as shown in Fig 1. Initially, an approximate position is estimated during the SPP processing phase by setting a higher elevation angle cutoff, which serves as a preliminary filter for potential candidate locations. Then, the approximate position is utilized as an observational center for mapping with the 3D building model to generate a sky mask, thereby aiding in the differentiation between NLOS and LOS satellites. Subsequently, the prior position and LOS satellites are fed into the PPP processing engine, supplemented by an optimized C/N₀-dependent stochastic model, to refine the smartphone's precise location and reduce the number of candidate position estimations required.

Algorithm 1 provides the pseudocode for 3D-mapping-aided NLOS/LOS satellite detection. Assuming that the smartphone can track I satellites at the approximate location, the elevation

set and azimuth set of all satellites are divided into $\mathbf{El} = \{El_1, El_2, \dots, El_I\}$ and $\mathbf{Az} = \{Az_1, Az_2, \dots, Az_I\}$. In addition, there are J buildings around the approximate location, and the edge coordinates of each building are stored in a 3D model database. Based on the sky mask of a smartphone at an approximate location, the elevation of the building edge corresponding to the azimuth of each satellite can be obtained. If the satellite elevation is lower than its corresponding building boundary area, the satellite is classified as NLOS; otherwise, it is classified as LOS. The sky mask derived from the approximate location and surrounding buildings can estimate the satellite visibility. By excluding NLOS satellites and using only LOS satellites for positioning, the large-ranging error caused by NLOS multipath can be mitigated, and the positioning performance of smartphones in urban environments can be guaranteed.

Algorithm 1 3D-mapping-aided NLOS/LOS satellites detection.

Input: Sky mask database, 3D building boundaries' elevations database $\mathbf{El}_b = \{El_{b,1}, El_{b,2}, \dots, El_{b,J}\}$ and azimuths database $\mathbf{Az}_b = \{Az_{b,1}, Az_{b,2}, \dots, Az_{b,J}\}$, satellite elevations database $\mathbf{El} = \{El_1, El_2, \dots, El_I\}$ and satellite azimuths database $\mathbf{Az} = \{Az_1, Az_2, \dots, Az_I\}$.

Output: NLOS satellites set \mathbf{L}_{NLOS} , LOS satellites set \mathbf{L}_{LOS}

```

1: // Satellites detection by 3D mapping matching
2: for  $i = 1 \rightarrow I$  do
3:   Obtain the satellite azimuth  $Az_i \in Az$  and the elevation  $El_i \in El$ 
4:   for  $j = 1 \rightarrow J$  do
5:      $\alpha_1 \leftarrow \min\{\mathbf{Az}_{b,j}\}$            // Minimum azimuth
6:      $\alpha_2 \leftarrow \max\{\mathbf{Az}_{b,j}\}$          // Maximum azimuth
7:     if  $\alpha_1 \leq Az_i \leq \alpha_2$  then
8:       Obtain the elevation  $El_{b,j}(Az_i)$  of building
9:       edge corresponding to the satellite azimuth  $Az_i$ 
10:      if  $El_i < El_{b,j}(Az_i)$  then
11:        add satellite  $i$  to  $\mathbf{L}_{NLOS}$  // NLOS satellite
12:      else if  $El_i \geq El_{b,j}(Az_i)$  then
13:        add satellite  $i$  to  $\mathbf{L}_{LOS}$  // LOS satellite
14:      else
15:        continue;
16:      end if
17:    end for
18:  end for
19: return  $\mathbf{L}_{NLOS}$  and  $\mathbf{L}_{LOS}$ 

```

C. Doppler Smoothing Filter Algorithm

As consumer-grade smartphones are equipped with ultra-low-cost GNSS antennas and chipsets, code pseudorange measurement errors will become more severe. If no processing is

performed on the pseudorange observations, the positioning accuracy will be minimal, even if the smartphone PPP technology is applied. As the ionosphere hardly changes between two adjacent epochs, we can then derive the classic Hatch filter equation as:

$$\bar{P}_{r,f}^{K,S}|_n = \frac{1}{n} P_{r,f}^{K,S}|_n + \left(1 - \frac{1}{n}\right) [\bar{P}_{r,f}^{K,S}|_{n-1} + (\phi_{r,f}^{K,S}|_n - \phi_{r,f}^{K,S}|_{n-1})] \quad (11)$$

However, to reduce the massive power consumption caused by continuous satellite tracking, smartphones typically use the duty cycle mechanism by default. In this mode, the tracking of the carrier phase becomes discontinuous [26]. Moreover, a small-sized patch antenna cannot resist multipath patterns, resulting in the introduction of more substantial multipath interference. This interference signal may lead to more frequent loss of lock and cycle slip in the carrier phase, significantly diminishing the performance of the hatch filter.

Compared with the carrier phase, Doppler observations are not affected by multipath and cycle slips and can guarantee high-precision continuous measurements in most cases. Therefore, we use Doppler shift instead of carrier phase for constant pseudorange smoothing. The change in the carrier phase between successive epochs is equivalent to the integration of the Doppler shift, and their relationship is as follows:

$$\begin{aligned} \phi_{r,f}^{K,S}|_n - \phi_{r,f}^{K,S}|_{n-1} &= \lambda_f^K \int_{t_{n-1}}^{t_n} D_{r,f}^{K,S}(t) dt \\ &= \frac{1}{2} \lambda_f^K T \cdot (D_{r,f}^{K,S}|_n + D_{r,f}^{K,S}|_{n-1}) \end{aligned} \quad (12)$$

where $D_{r,f}^{K,S}|_n$ and $D_{r,f}^{K,S}|_{n-1}$ denote the Doppler shift observations at epoch n and $n - 1$, respectively; T represents the time interval between adjacent epochs, that is, the data sampling rate. In addition, with the gradual increase of smoothing epochs, the ionospheric accumulation error will gradually become larger and cannot be ignored. When the ionospheric cumulative error exceeds the accuracy of pseudorange measurement, pseudorange smoothing will become meaningless. Therefore, the number n of smoothing epochs must be limited to prevent the ionospheric cumulative error from increasing infinitely.

Assuming that the effective window of the Doppler smoothing pseudorange is W , the smoothing epoch n is fixed at the window width when the number of smoothing epochs exceeds it. Therefore, the Doppler smoothing filter (DSF) considering the ionospheric cumulative error can be expressed as:

$$\begin{cases} \bar{P}_{r,f}^{K,S}|_n = P_{r,f}^{K,S}|_n, \quad n = 1 \quad || \quad \left(|P_{r,f}^{K,S}|_n - \bar{P}_{r,f}^{K,S}|_n| > \xi_{P_{r,f}^{K,S}}\right) \quad || \quad \left(|D_{r,f}^{K,S}|_{n+2} - 2D_{r,f}^{K,S}|_{n+1} + D_{r,f}^{K,S}|_n| > \xi_{D_{r,f}^{K,S}}\right) \\ \bar{P}_{r,f}^{K,S}|_n = \frac{1}{n} P_{r,f}^{K,S}|_n + \left(1 - \frac{1}{n}\right) \left[\bar{P}_{r,f}^{K,S}|_{n-1} + \frac{1}{2} \lambda_f^K T \cdot (D_{r,f}^{K,S}|_n + D_{r,f}^{K,S}|_{n-1})\right], \quad 1 < n \leq W \\ \bar{P}_{r,f}^{K,S}|_n = \frac{1}{W} P_{r,f}^{K,S}|_n + \left(1 - \frac{1}{W}\right) \left[\bar{P}_{r,f}^{K,S}|_{n-1} + \frac{1}{2} \lambda_f^K T \cdot (D_{r,f}^{K,S}|_n + D_{r,f}^{K,S}|_{n-1})\right], \quad n > W \end{cases} \quad (13)$$

When $|P_{r,f}^{K,S}|_n - \bar{P}_{r,f}^{K,S}|_n| > \xi_{P_{r,f}^K}$, it means that the accumulative ionospheric error has exceeded the normal range of the pseudorange measurement error, and the filter needs to be reinitialized at this time. In addition, possible outliers in the Doppler shift must be considered to improve the filter robustness. The second-difference Doppler shift between epochs can reflect the Doppler measurement error, and the filter needs to be reinitialized when $|D_{r,f}^{K,S}|_{n+2} - 2D_{r,f}^{K,S}|_{n+1} + D_{r,f}^{K,S}|_n| > \xi_{D_{r,f}^K}$. According to the error propagation law of variance and covariance, the thresholds $\xi_{P_{r,f}^K}$ and $\xi_{D_{r,f}^K}$ should be three times the observation noise, that is, $\xi_{P_{r,f}^K} = 3\varepsilon_{P_{r,f}^K}$ and $\xi_{D_{r,f}^K} = 3\varepsilon_{D_{r,f}^K}$. The smoothing window W is set to 25 for low-cost smart devices. This proposed DSF algorithm significantly mitigates the impact of LOS multipath errors and irregular pseudorange measurements by considering ionospheric cumulative errors, thus ensuring continuous and accurate pseudorange smoothing without introducing additional errors.

D. Optimized C/N₀-Dependent Stochastic Model

Since the GNSS constellation is distributed across different orbits, the receiver on the ground observes that each satellite has a different elevation and orientation. Considering the impact of buildings, trees, and various interference signals on GNSS signals, the observation quality of different satellites varies significantly [27]. Therefore, the weights of the different satellites should be considered when calculating the parameters to be estimated in (7), which is the GNSS stochastic model. The weighted matrix \mathbf{P} corresponding to the carrier phase and pseudorange observations of dual-frequency GNSS smartphones can be expressed as follows:

$$\mathbf{P}_r^{K,S} = \begin{bmatrix} \sigma_{P_{r,1}^{K,S}}^{-2} & & & \\ & \sigma_{\phi_{r,1}^{K,S}}^{-2} & & \\ & & \sigma_{P_{r,5}^{K,S}}^{-2} & \\ & & & \sigma_{\phi_{r,5}^{K,S}}^{-2} \end{bmatrix} \quad (14)$$

where σ^2 represents the variance of pseudorange or carrier phase observations; K , s , and r represent the satellite system, space vehicle number, and receiver, respectively, and they are consistent with the meanings in Section III-A. The weighting matrix is a diagonal matrix, meaning that all non-diagonal elements are zeros. This design ensures that each observation is independently weighted according to its variance, which enhances the robustness and accuracy of the positioning algorithm.

Internationally well-known GNSS processing software (such as Bernese [28], GAMIT [29] and GSTAR [18]) usually uses elevation-dependent stochastic models to calculate the weighted variance. However, low-cost smartphones have built-in passive linearly polarized microstrip antennas, which render the satellite elevation-dependent stochastic model useless. Previous studies have shown that C/N₀ is an effective indicator of

GNSS signal quality and that a C/N₀-dependent stochastic model can be applied to smartphone observations [22]. However, there is a large variability in the observations measured by dual-band smartphones at the two frequencies, which is not accounted for in classical C/N₀-dependent stochastic models. Therefore, this study proposes an optimized C/N₀-dependent stochastic model for low-cost smartphones:

$$\left\{ \begin{array}{l} \sigma_{P_{r,1}^{K,S}}^2 = \varepsilon_{P_1}^2 \cdot \left(a_{r,1}^K + b_{r,1}^K \cdot 10^{-\frac{C/N_{0,r,1}^{K,S}}{10}} \right) \\ \sigma_{\phi_{r,1}^{K,S}}^2 = \varepsilon_{\phi_1}^2 \cdot \left(a_{r,1}^K + b_{r,1}^K \cdot 10^{-\frac{C/N_{0,r,1}^{K,S}}{10}} \right) \\ \sigma_{P_{r,5}^{K,S}}^2 = \varepsilon_{P_5}^2 \cdot \left(a_{r,5}^K + b_{r,5}^K \cdot 10^{-\frac{C/N_{0,r,5}^{K,S}}{10}} \right) \\ \sigma_{\phi_{r,5}^{K,S}}^2 = \varepsilon_{\phi_5}^2 \cdot \left(a_{r,5}^K + b_{r,5}^K \cdot 10^{-\frac{C/N_{0,r,5}^{K,S}}{10}} \right) \end{array} \right. \quad (15)$$

where $C/N_{0,r,1}^{K,S}$ and $C/N_{0,r,5}^{K,S}$ represent the C/N₀ of the satellite signal on the L1 frequency and the L5 frequency, respectively; ε_{P_1} and ε_{ϕ_1} represent the standard deviations of the observation noise of the pseudorange and carrier phase on the L1 frequency, respectively, and are taken as 2.0 and 0.01 for smartphones in this study; ε_{P_5} and ε_{ϕ_5} represent the standard deviations of the observation noise of the pseudorange and carrier phase on the L5 frequency, respectively, and are taken as 1.0 and 0.01 for smartphones in this study; and $a_{r,1}^K$, $b_{r,1}^K$, $a_{r,5}^K$ and $b_{r,5}^K$ are the coefficients of the optimized stochastic model, and the coefficients are calibrated in Section IV-D.

Equation (15) represents the crux of the proposed stochastic model for dual-frequency GNSS observations in smartphones, specifically leveraging the L1 and L5 frequencies. The model accounts for the variable quality of GNSS signals received by smartphones by adjusting the observation noise variance based on the C/N₀ for each frequency. This approach is instrumental in accommodating the inherent variability in signal quality due to factors like multipath effects, signal obstructions, and atmospheric conditions, which are particularly pronounced in urban environments. This tailored model enhances the precision of GNSS positioning calculations by providing a more nuanced treatment of observation noise, contributing to the overall robustness and accuracy of our positioning solution.

IV. EXPERIMENTS AND ANALYSIS

In this section, we describe the design of static and kinematic experiments to evaluate the performance of the proposed method. Section IV-A describes the specific experimental setup. Section IV-B verifies the effectiveness of the 3D-mapping-aided NLOS/LOS satellite detection algorithm. Section IV-C analyzes the performance of the Doppler smoothing filter algorithm. Section IV-D determines the parameters of the optimized C/N₀-dependent stochastic model. Section IV-E discusses the positioning accuracy of the two sets of experiments

in detail.

A. Static and Kinematic Experiment Setup

Static and kinematic experiments are conducted to comprehensively evaluate and verify the performance of the proposed algorithm. The experimental site was a large teaching building in a university in Beijing. The building has a rectangular structure and covers an area of 226,000 m². The building has a protruding architecture with mixed concrete glass curtain walls protruding on all sides, which more realistically reflects signal propagation in urban areas. In addition, the 3D models of this large building were generated by a professional mapping company, and there were almost no coordinate errors.

Fig. 3 shows the kinematic experiment, static experiment and experimental devices, respectively. All devices in the kinematic experiment were placed on an unmanned ground vehicle (SCOUT 2.0-UGV) produced by AGILEX and driven around the teaching building. In the static experiment, all the devices were statically placed in the middle of the building to record the observation data. The experimental device saved the raw GNSS observation data for all constellations and frequencies supported by its chipset at 1 Hz.

The BUAA RINEX Converter (<https://github.com/Jia-le-wang/BUAA-RINEX-Converter>) developed in this study is used to convert raw GNSS measurements from smartphones into standard RINEX 3.05 data, including the pseudorange, carrier phase, Doppler shift, and C/N₀. This tool addresses and rectifies several bugs that were present in other software tools, such as inconsistencies between Doppler and carrier phase data in the GEO++ software, misalignment between pseudorange and phase clocks, as well as the confusion between BDS B1C and B1I signals, among others. These enhancements significantly aid researchers by circumventing peculiar issues that may arise due to conversion software, thereby ensuring the integrity and reliability of their data processing and analysis.

wang/BUAA-RINEX-Converter) developed in this study is used to convert raw GNSS measurements from smartphones into standard RINEX 3.05 data, including the pseudorange, carrier phase, Doppler shift, and C/N₀. This tool addresses and rectifies several bugs that were present in other software tools, such as inconsistencies between Doppler and carrier phase data in the GEO++ software, misalignment between pseudorange and phase clocks, as well as the confusion between BDS B1C and B1I signals, among others. These enhancements significantly aid researchers by circumventing peculiar issues that may arise due to conversion software, thereby ensuring the integrity and reliability of their data processing and analysis.

The devices used in the experiment included three consumer-grade smartphones—Xiaomi Mi8 and Huawei Mate40, as well as low-cost u-blox ZED-F9P and Septentrio Mosaic-X5 receivers for comparative analysis. The experimental devices used in this study and their related characteristics are listed in Table I in detail. In addition, the reference positions of all devices in the experiment were provided by the Vision-RTK equipment after the error correction of the lever arm. Vision-RTK was produced by a cutting-edge Swiss technology company called Fixposition. It integrates a dual-antenna RTK, camera, and an inertial system to provide a global centimeter-level positioning trajectory [30].

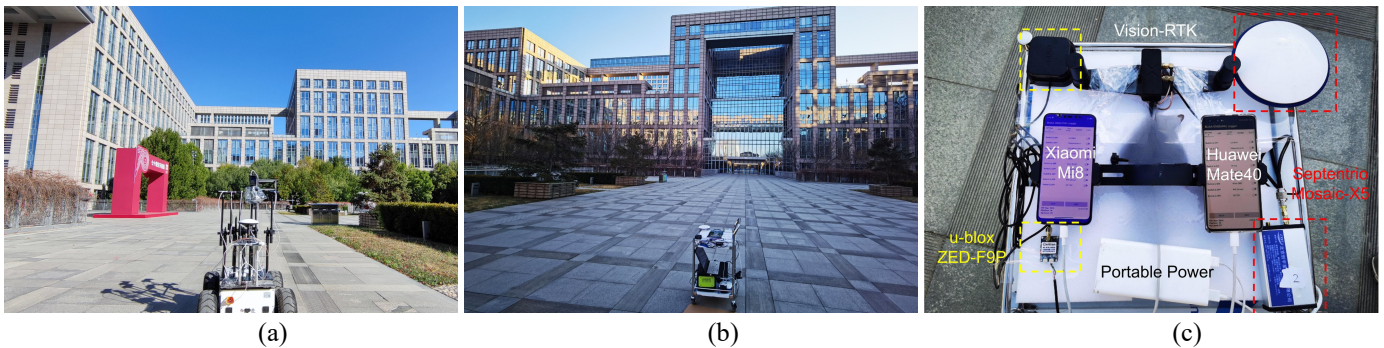


Fig. 3. Kinematic and static experiment scenarios and all devices used in the experiments. (a) Kinematic experiment. (b) Static experiment. (c) Experimental devices and their annotation.

TABLE I
EXPERIMENTAL DEVICES AND RELATED CHARACTERISTICS

Device (SoC)	Antenna	Constellation availability	Frequency availability	Phase availability
Xiaomi Mi8 (Broadcom BCM47755)	LP	GPS/GLONASS/BDS/GALILEO/QZSS	Dual-frequency L1+L5	Yes
Huawei Mate40 (HiSilicon Kirin 9000)	LP	GPS/GLONASS/BDS/GALILEO/QZSS	Dual-frequency L1+L5	Yes
u-blox ZED-F9P	RHCP	GPS/GLONASS/BDS/GALILEO/QZSS	Dual-frequency L1+L2	Yes
Septentrio Mosaic-X5	RHCP	GPS/GLONASS/BDS/GALILEO/QZSS	Multi-frequency L1+L2+L5	Yes

“LP” represents “Linearly Polarized,” “RHCP” represents “Right-Handed Circularly Polarized,” and “SoC” indicates the “System on Chip.”

B. NLOS/LOS Satellite Classification by 3D Mapping

To verify the effectiveness of the 3DMA detection algorithm,

we analyzed the GNSS data collected through static and kinematic experiments in detail. Fig. 4 shows the statistics of the normalized probability distribution of C/N₀ of LOS and NLOS

signals tracked by smart devices. It can be seen from the figure that it is not easy to directly distinguish LOS and NLOS signals simply by C/N_0 , even though LOS signals are often distributed in a higher signal strength range than NLOS signals. The LOS signals of the two smartphones are mainly distributed at 30–40 dB-Hz.

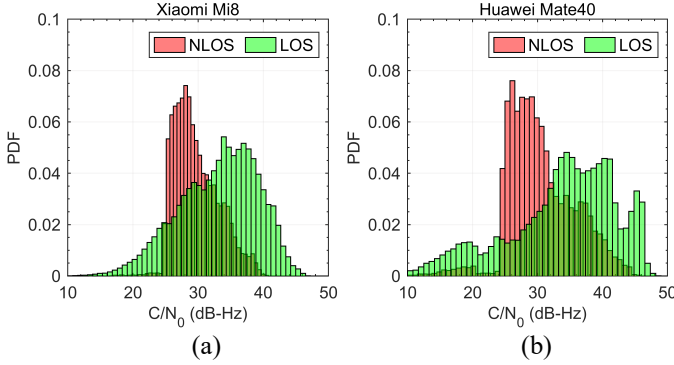


Fig. 4. Normalized probability distribution of C/N_0 for LOS and NLOS signals. (a) Xiaomi Mi8. (b) Huawei Mate40.

The 3DMA detection algorithm can accurately predict the satellite visibility when both the approximate location and 3D building model are accurate. To visually display the satellite detection results, Figs. 5 and 6 show the distributions of LOS and NLOS satellites in the static and kinematic scene under a specific epoch. The gray area is the occlusion area of the building, the green dot is the LOS satellite, and the red dot is the NLOS satellite. Clearly, in urban areas with significant building obstructions, our detection algorithm can accurately identify NLOS and LOS satellites, which can be promptly excluded from the PPP processing.

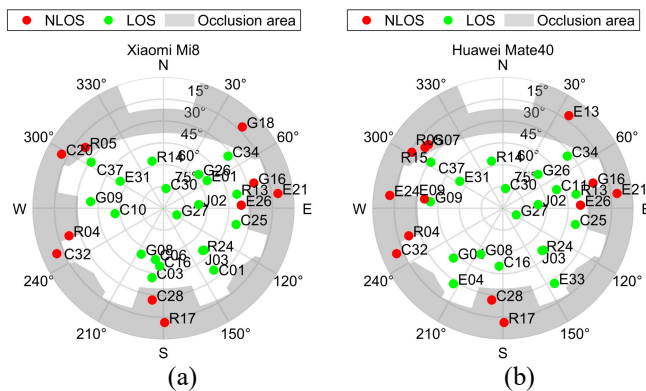


Fig. 5. Distribution of LOS and NLOS satellites in the static scene under a specific epoch. (a) Xiaomi Mi8. (b) Huawei Mate40

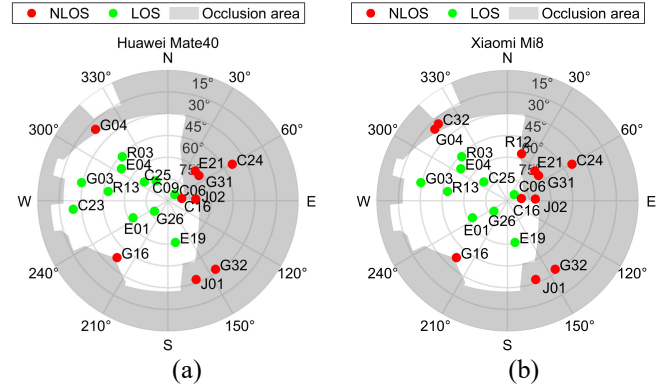
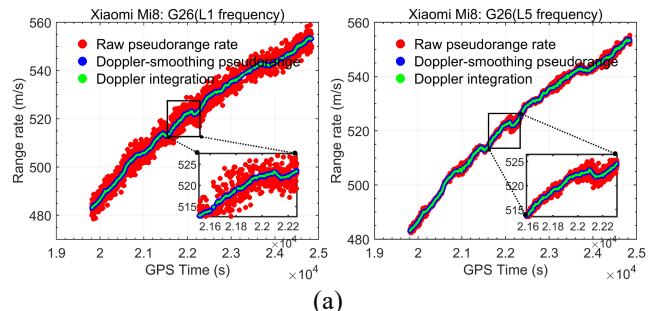


Fig. 6. Distribution of LOS and NLOS satellites in the kinematic scene under a specific epoch. (a) Xiaomi Mi8. (b) Huawei Mate40

C. Performance Analysis of Doppler Smoothing Filter Algorithm

Smartphones are equipped with small-sized microstrip antennas and ultra-low-cost chipsets, which lead to more severe multipath and thermal noise in the code pseudorange observations. The 3DMA algorithm can accurately detect NLOS multipath and exclude them from PPP processing, where the LOS multipath and thermal noise must be mitigated by the proposed Doppler smoothing filter (DSF) algorithm. Since the Doppler integration between epochs equals the pseudorange rate, Doppler can be used as a reference to reflect the pseudorange measurement error. Taking the L1 and L5 frequencies of the GPS G26 satellite as an example, Fig. 7 shows the measurement error comparison between the raw pseudorange rate and the Doppler-smoothing pseudorange of smart devices. As can be seen from the figure, the pseudorange observation has a more significant measurement error than the Doppler observation for smartphones. In addition, the L5 signal with a chipping rate increased by ten times is more resistant to the frequency-selective fading caused by the multipath effect; therefore, the pseudorange measurement error on the L5 frequency is significantly smaller than that on the L1 frequency. Encouragingly, after applying the DSF algorithm, the pseudorange measurement error was reduced to a level nearly consistent with the Doppler measurement error (blue and green curves).



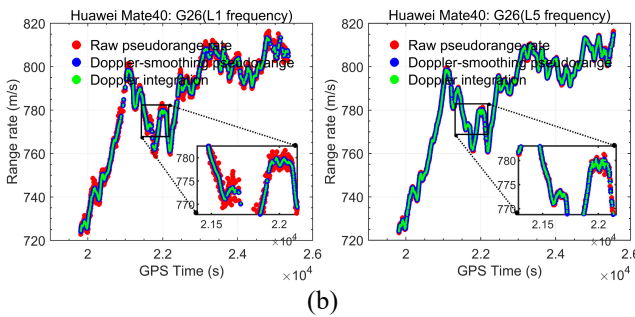


Fig. 7. Comparison of pseudorange measurement errors at L1 and L5 frequencies before and after applying the Doppler smoothing filter. (a) Xiaomi Mi8. (b) Huawei Mate40.

TABLE II summarizes the pseudorange measurement errors before and after the application of the DSF algorithm. Overall, the DSF algorithm can mitigate more than 70% of the pseudorange measurement errors, including LOS multipath and chip thermal noise. In particular, errors were suppressed to a greater degree for consumer-grade smartphones. For example, the raw pseudorange measurement error on the L1 frequency of Xiaomi Mi8 is as high as 2.2 m, while the measurement error using DSF is only 0.15 m and is reduced by 93.18%. The DSF algorithm can effectively reduce the pseudorange measurement error, which helps to improve the positioning accuracy and initialization speed for SPP and PPP processing.

TABLE II

SUMMARY OF DOPPLER SMOOTHING FILTER ALGORITHM IN REDUCING PSEUDORANGE MEASUREMENT ERROR

Device and frequency	Raw	Smoothed	Reduced
	RMS error (m)	Percent (%)	
Xiaomi Mi8	L1 2.20	0.15	93.18
	L5 0.57	0.10	82.46
Huawei Mate40	L1 1.19	0.13	89.08
	L5 0.42	0.11	73.81
u-blox ZED-F9P	L1 0.37	0.07	81.08
	L2 0.34	0.09	73.53
Septentrio	L1 0.28	0.06	78.57
Mosaic-X5	L5 0.26	0.06	76.92

D. Coefficients Calibration of Optimized C/N₀-Dependent Stochastic Model

A stochastic model is vital for determining the observation weights and positioning accuracies of different satellites. In Section III-D, we propose an optimized C/N₀-dependent stochastic model suitable for smartphones. The coefficients of the C/N₀-dependent stochastic model were calibrated using the short-baseline inter-station single-difference (SD) model [31]. The survey-grade receiver was selected as the reference station, and the static coordinates of the smartphone and receiver were fixed, such that pseudorange residuals could be obtained

through the inter-station single-difference model. Using the B1I frequency of the BDS C30 satellite as an example, Fig. 8 shows the relationship between the pseudorange SD residual, elevation, and C/N₀. It can be seen that the SD residuals of the Xiaomi Mi8 and Huawei Mate40 equipped with linearly polarized antennas only maintain a correlation with C/N₀, and the residuals increase sharply when C/N₀ decreases.

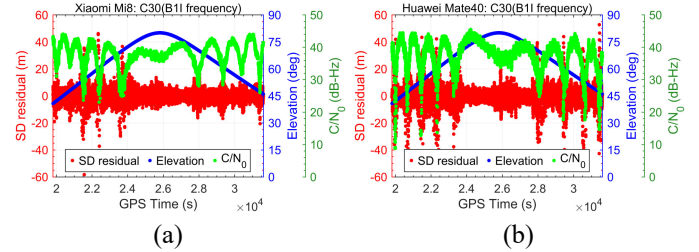


Fig. 8. Relationship between pseudorange SD residual, elevation angle, and C/N₀. (a) Xiaomi Mi8. (b) Huawei Mate40.

The Pearson correlation coefficient (PCC) is most commonly used to measure the correlation between two random variables, and its value ranges from -1 to 1. Assuming that the correlation coefficient between two variables is PCC , when $|PCC| < 0.3$, the variables are almost irrelevant; when $0.3 \leq |PCC| < 0.5$, the variables are moderately correlated, and when $|PCC| \geq 0.5$, the variables have a strong correlation [32]. Fig. 9 shows a PCC heat map of the SD residuals, elevation, and C/N₀. The results show that the $|PCC|$ of the SD residual and C/N₀ exceeds 0.5 for both smartphones, but the $|PCC|$ of the SD residual and elevation is less than 0.3. The statistical results indicate that the measurement error of smartphones has a strong correlation only with C/N₀. Therefore, the C/N₀-dependent stochastic model is more suitable to weigh smartphone GNSS measurements.

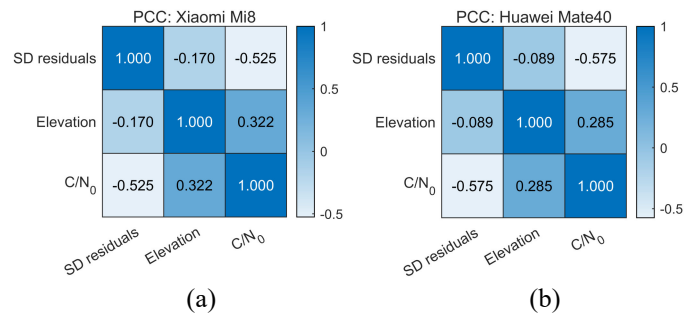


Fig. 9. Pearson correlation coefficient (PCC) heat map between SD residuals, elevation, and C/N₀. (a) Xiaomi Mi8. (b) Huawei Mate40.

Taking the Huawei Mate40 as an example, Fig. 10 shows the fitted coefficients according to the optimized C/N₀-dependent stochastic model shown in (23). We calibrated the coefficients of all the constellations and frequencies supported by the experimental devices to reflect the GNSS measurement error characteristics more comprehensively, including GPS (L1+L5), GLONASS (G1), BDS (B1), GALILEO (E1+E5a), and QZSS

(L1+L5). Table III summarizes the fitted coefficients of the optimized C/N₀-dependent stochastic models for the four experimental devices. The stochastic model coefficients need to be

calibrated only once for each device and can be applied to subsequent algorithm processing. Additionally, a C/N₀ threshold (e.g., 20 dB-Hz) can be set in PPP processing to limit outlier observations due to low signal strength.

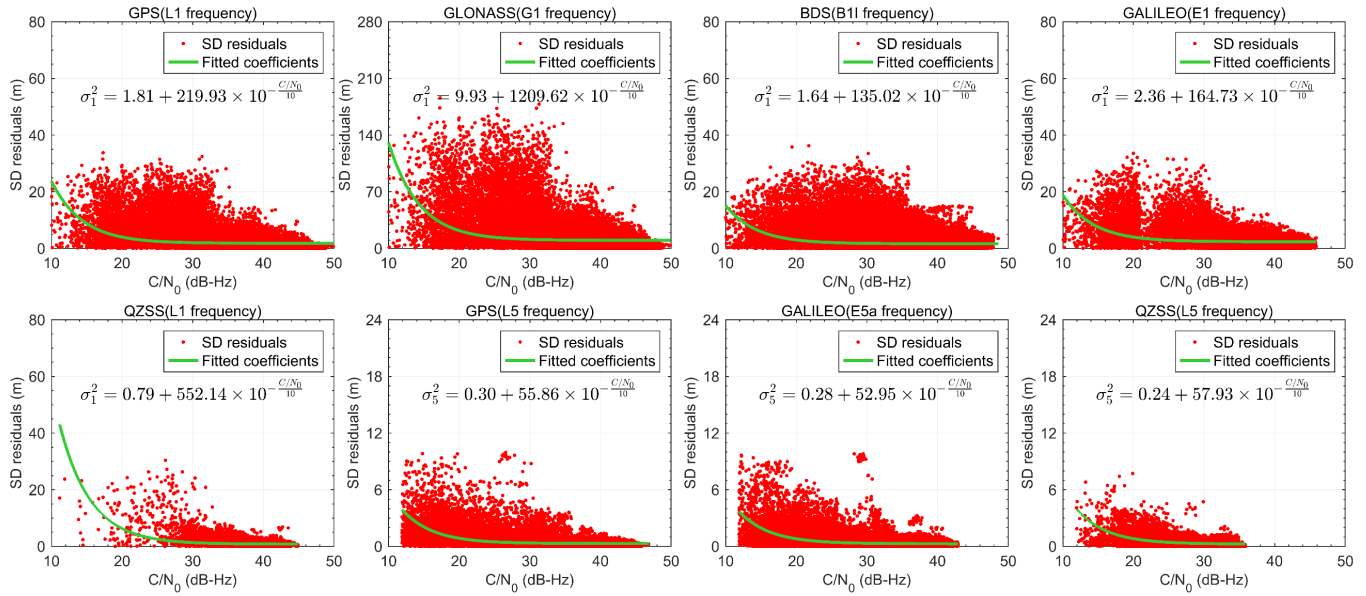


Fig. 10. Fitted coefficients of the optimized C/N₀-dependent stochastic model for each constellation and frequency, taking the Huawei Mate40 smartphone as an example.

TABLE III
FITTED COEFFICIENTS OF THE OPTIMIZED C/N₀-DEPENDENT STOCHASTIC MODELS FOR DIFFERENT DEVICES

Constellation and frequency	Xiaomi Mi8		Huawei Mate40		u-blox ZED-F9P		Septentrio Mosaic-X5		
	a	b	a	b	a	b	a	b	
GPS	L1	2.94	2536.86	1.81	219.93	0.09	826.66	0.06	718.18
	L5	0.27	538.20	0.30	55.86	0.12	291.38	0.08	245.75
GLONASS	G1	11.21	1909.85	9.93	1209.62	0.32	770.82	0.20	698.31
BDS	B1I	1.46	2557.65	1.64	135.02	0.14	684.74	0.09	597.48
GALILEO	E1	1.97	2170.74	2.36	164.73	0.11	1282.16	0.07	1198.53
	E5a	0.29	249.90	0.28	52.95	0.12	312.08	0.08	259.76
QZSS	L1	2.21	3478.41	0.79	552.14	0.13	1538.59	0.09	1438.24
	L5	0.17	320.74	0.24	57.93	0.14	374.49	0.10	311.72

E. Positioning Result Analysis

To better reflect the effectiveness of the proposed algorithm, we evaluate the positioning results of four strategies: Conventional PPP, 3DMA PPP, 3DMA PPP+DSF, and 3DMA PPP+DSF+C/N₀ SM (C/N₀-dependent stochastic model). Accurately assessing positioning performance under real-world conditions, we applied a kinematic solution approach to the PPP processing in both static and kinematic experiments. This approach ensured that the process noise associated with position estimates in the static experiments remained consistent with that of the kinematic experiments, rather than imposing stricter constraints on the position estimates. This methodological

choice was made to ensure that the PPP algorithm's performance is evaluated in conditions that closely mimic those encountered during actual device usage, providing a realistic assessment of its efficacy across different scenarios.

The positioning solutions of different GNSS-degraded receivers in the static and kinematic experiments are shown in Figs. 11 and 12, respectively. The positioning results show that the conventional PPP algorithm performs worst, and the deviation from the ground truth is the largest in both the static and kinematic experiments. After excluding NLOS satellites using the 3DMA PPP algorithm, the positioning results of all devices were significantly improved. Furthermore, after reducing the

potential LOS multipath errors using the DSF algorithm and C/N₀ SM algorithm, all positioning trajectories remain consistent with the ground truth.

The box plots in Fig. 13(a) and (b) show the statistical characteristics of the positioning error of each device when using different positioning strategies in the static and kinematic experiments. The box plot can reflect the dispersion of positioning errors and provide multiple statistical summaries, such as the maximum, minimum, and median, as well as intuitive data vis-

ualization (as shown in Fig. 13(c)). The positioning results indicate that the NLOS signals generated by building obstructions will significantly degrade the GNSS positioning performance. Suppose NLOS satellites cannot be identified effectively. In that case, the positioning error of smartphones may even exceed 10 m when using the conventional PPP algorithm, which is far from satisfying the demand for high-precision location services. After adopting the improved algorithm proposed in this study, the GNSS positioning performance of low-cost smartphones and receivers is greatly improved.

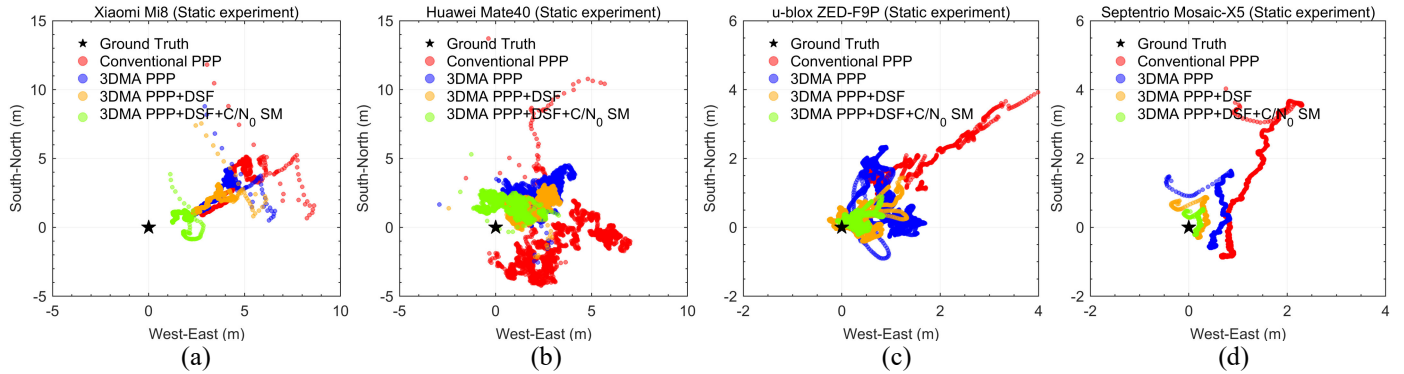


Fig. 11. Positioning solutions for each device using different strategies in the static experiment. (a) Xiaomi Mi8. (b) Huawei Mate40. (c) u-blox ZED-F9P. (d) Septentrio Mosaic-X5.

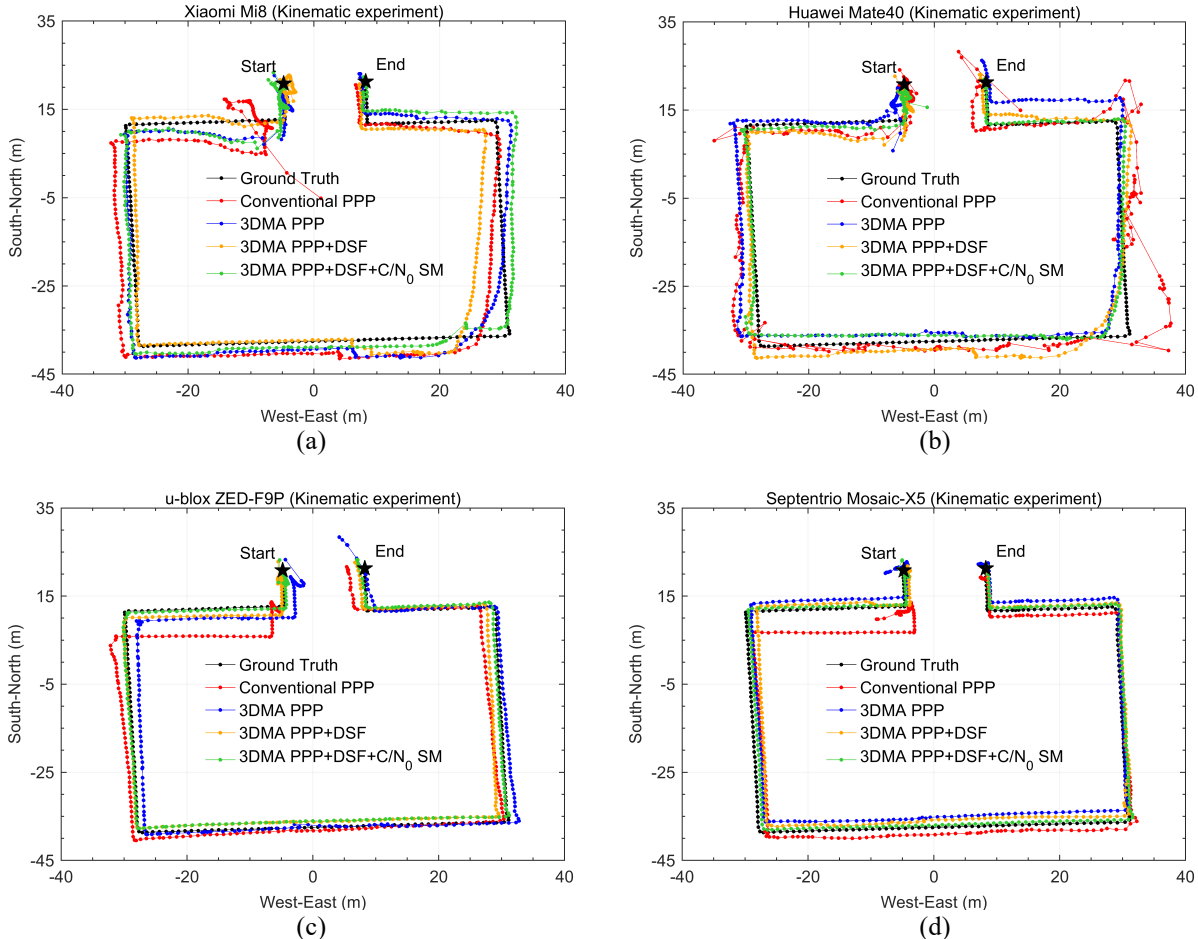


Fig. 12. Positioning solutions for each device using different strategies in the kinematic experiment. (a) Xiaomi Mi8. (b) Huawei Mate40. (c) u-blox ZED-F9P. (d) Septentrio Mosaic-X5.

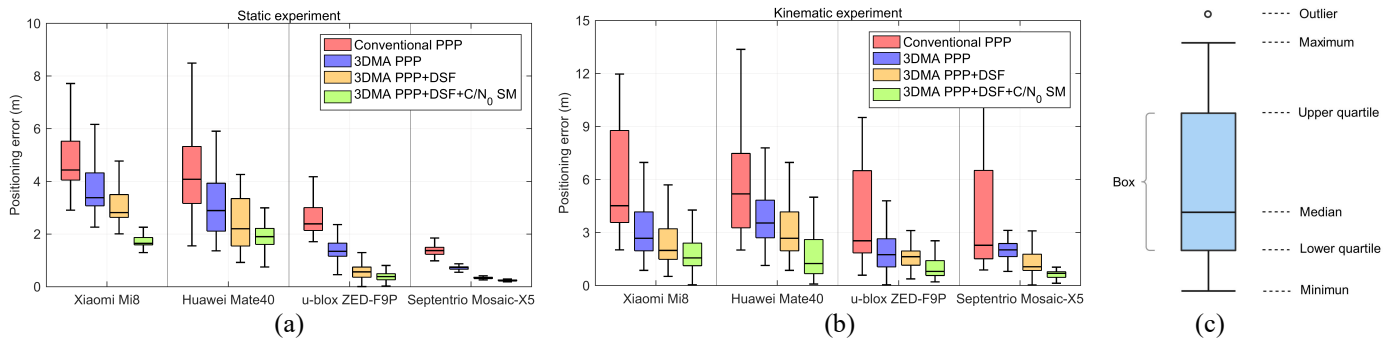


Fig. 13. Box plots generated by positioning errors of each device under different strategies. (a) Box plot of the static experiment. (b) Box plot of the kinematic experiment. (c) Box plot interpretation.

Table IV summarizes the statistical analyses of the positioning errors under the four strategies, including the minimum (Min), maximum (Max), Root Mean Square (RMS), and median (Med) errors. The results show that the static positioning error of the Xiaomi Mi8 based on RMS statistics using the proposed algorithm decreases from 4.87 m to 1.71 m, and the kinematic positioning error decreases from 6.40 m to 1.76 m. Compared with the conventional PPP algorithm, the positioning performance has been improved by 64.89% and 72.50%, respectively. Similarly, after applying the algorithm proposed in this study, the positioning error of Huawei Mate40 based on the RMS statistics in the static and kinematic experiments was better than 1.95 m and 1.93 m, respectively. Compared to the conventional PPP algorithm, the positioning performance improved by 55.48% and 68.67%, respectively.

In addition, the proposed algorithm is suitable for low-cost

GNSS receivers, and the improvement is significant. u-blox ZED-F9P achieves static RMS errors of 1.73 m, 1.46 m, 0.60 m, and 0.40 m under four positioning strategies, while Septentrio Mosaic-X5 can achieve a positioning accuracy of up to 0.23 m. In the kinematic experiments, the positioning accuracy of the two GNSS receivers also showed significant improvement. Compared to the conventional PPP algorithm, u-blox ZED-F9P and Septentrio Mosaic-X5 improved their positioning accuracies by 80.64% and 85.86%, respectively, after using the algorithm in the kinematic experiment. Similarly, the proposed algorithm significantly reduces the maximum error. For example, the maximum kinematic positioning error of Xiaomi Mi8 and Huawei Mate40 is reduced from 11.97 m and 13.37 m to 4.27 m and 5.00 m, respectively, which dramatically improves the navigation experience.

TABLE IV
SUMMARY OF MULTIPLE STATISTICAL INDICATORS OF STATIC AND KINEMATIC POSITIONING ERRORS

Devices and positioning strategies	Static positioning error (m)				Kinematic positioning error (m)				
	Min	Max	RMS	Med	Min	Max	RMS	Med	
Xiaomi Mi8	Conventional PPP	2.91	7.72	4.87	4.42	2.00	11.97	6.40	4.48
	3DMA PPP	2.26	6.17	3.82	3.38	0.86	6.97	3.31	2.22
	3DMA PPP+DSF	2.01	4.77	3.11	2.81	0.52	5.70	2.79	1.98
	3DMA PPP+DSF+C/N ₀ SM	1.29	2.26	1.71	1.64	0.14	4.27	1.76	1.39
Huawei Mate40	Conventional PPP	1.55	8.49	4.38	4.06	2.02	13.37	6.16	4.92
	3DMA PPP	1.36	5.90	3.31	2.89	1.13	7.79	3.91	3.54
	3DMA PPP+DSF	0.92	4.26	2.57	2.20	0.86	6.97	3.31	2.55
	3DMA PPP+DSF+C/N ₀ SM	0.75	2.99	1.95	1.89	0.08	5.00	1.93	1.23
u-blox ZED-F9P	Conventional PPP	1.21	2.99	1.73	1.62	0.88	11.84	5.01	2.28
	3DMA PPP	0.46	2.36	1.46	1.34	0.15	4.80	2.13	1.73
	3DMA PPP+DSF	0.12	1.29	0.60	0.55	0.35	3.11	1.62	1.62
	3DMA PPP+DSF+C/N ₀ SM	0.07	0.81	0.40	0.38	0.19	2.53	0.97	0.78
Septentrio Mosaic-X5	Conventional PPP	0.98	1.85	1.31	1.35	0.58	9.51	4.67	2.53
	3DMA PPP	0.55	0.87	0.71	0.72	0.80	3.12	2.05	2.02
	3DMA PPP+DSF	0.25	0.41	0.34	0.34	0.08	3.09	1.37	1.06
	3DMA PPP+DSF+C/N ₀ SM	0.18	0.29	0.23	0.24	0.13	1.04	0.66	0.69

V. CONCLUSION AND OUTLOOK

Precise positioning in GNSS-degraded areas has always been a problem that plagues the industry, especially for consumer-grade smartphones that can only be equipped with linearly polarized patch antennas. Urban buildings can easily cause occlusion, refraction, and reflection of GNSS signals. It is often challenging to model multipath effectively or identify satellites that interfere with the raw signals in the real world. GNSS observations that absorb NLOS and LOS multipath errors lead to large errors in the positioning solution or even the inability to complete the positioning process.

To improve the positioning performance of smartphones in GNSS-degraded environments, this study presents a 3D-mapping-aided precision point positioning algorithm. First, all satellites are classified into NLOS and LOS satellites based on the sky masks generated by 3D building models. Since NLOS reception causes large-ranging errors, we exclude NLOS satellites from PPP processing to avoid deteriorating the positioning solution. Second, we propose a Doppler smoothing filter algorithm for potential multipath errors in LOS satellites that considers the ionospheric cumulative error, which can mitigate more than 70% of thermal noise and multipath error. Finally, correlation analysis shows that the measurement error of smartphone GNSS maintains a strong correlation only with C/N₀. Therefore, a C/N₀-dependent stochastic model is constructed to reasonably reweight the LOS satellites.

To verify the effectiveness of the proposed algorithm, kinematic vehicle, and static experiments were conducted in an urban area with 3D building models. The results show that the overall positioning performance of the proposed algorithm is improved by more than 50% compared with the conventional PPP algorithm. Whether it is a static or a kinematic vehicle scene, the positioning error of Xiaomi Mi8 and Huawei Mate40 smartphones drops from more than 5 m to 1–2 m, where the low-cost u-blox ZED-F9P and Septentrio Mosaic-X5 receivers achieve sub-meter level positioning accuracy. The proposed algorithm is expected to provide high-precision positioning capabilities for low-cost smart devices. Future research will incorporate additional sensors from consumer-grade smartphones, such as accelerometers, gyroscopes, magnetometers, and barometers, to significantly enhance the system's adaptability to signal blockage and multipath effects, especially in urban canyons and indoor environments, ensuring a seamless navigation experience.

REFERENCES

- [1] H. Chen, M. Xiao, and Z. Pang, "Satellite-Based Computing Networks with Federated Learning," *IEEE Wireless Commun.*, vol. 29, no. 1, pp. 78-84, Feb. 2022.
- [2] X. Fang, L. Xie, and X. Li, "Integrated Relative-Measurement-Based Network Localization and Formation Maneuver Control," *IEEE Trans. Autom. Control*, vol. 69, no. 3, pp. 1906-1913, Mar. 2024.
- [3] X. Fang, and L. Xie, "Distributed Formation Maneuver Control Using Complex Laplacian," *IEEE Trans. Autom. Control*, vol. 69, no. 3, pp. 1850-1857, Mar. 2024.
- [4] L. Liu, Z. Zhou, F. Zhou, and X. Shi, "A New 3-D Geometry Reconstruction Method of Space Target Utilizing the Scatterer Energy Accumulation of ISAR Image Sequence," *IEEE Trans. Geosci. Remote Sens.*, vol. 58, no. 12, pp. 8345-8357, Dec. 2020.
- [5] L. Liu, F. Zhou, M. Tao, P. Sun, and Z. Zhang, "Adaptive Translational Motion Compensation Method for ISAR Imaging Under Low SNR Based on Particle Swarm Optimization," *IEEE J. Sel. Top. Appl. Earth Obs. Remote Sens.*, vol. 8, no. 11, pp. 5146-5157, Nov. 2015.
- [6] F. Jin, K. Liu, C. Liu, T. Cheng, H. Zhang, and V. C. S. Lee, "A Cooperative Vehicle Localization and Trajectory Prediction Framework Based on Belief Propagation and Transformer Model," *IEEE Trans. Consum. Electron.*, vol. 70, no. 1, pp. 2746-2758, Feb. 2024.
- [7] G. M. Fu, M. Khider, and F. van Diggelen, "Android raw GNSS measurement datasets for precise positioning," *Proceedings of the 33rd international technical meeting of the satellite division of the Institute of Navigation (ION GNSS+ 2020)*, pp. 1925-1937. 2020.
- [8] A. Iqbal, M. N. Aman, and B. Sikdar, "Machine and Representation Learning-Based GNSS Spoofing Detectors Utilizing Feature Set From Generic GNSS Receivers," *IEEE Trans. Consum. Electron.*, vol. 70, no. 1, pp. 574-583, Feb. 2024.
- [9] P. D. Groves, and M. Adjrad, "Performance assessment of 3D-mapping-aided GNSS part 1: Algorithms, user equipment, and review," *NAVIGATION*, vol. 66, no. 2, pp. 341-362, Jun. 2019.
- [10] H.-F. Ng, G. Zhang, Y. Luo, and L.-T. Hsu, "Urban positioning: 3D mapping-aided GNSS using dual-frequency pseudorange measurements from smartphones," *NAVIGATION*, vol. 68, no. 4, pp. 727-749, 2021/12/01. 2021.
- [11] W. Wen, X. Bai, Y. C. Kan, and L.-T. Hsu, "Tightly Coupled GNSS/INS Integration via Factor Graph and Aided by Fish-Eye Camera," *IEEE Trans. Veh. Technol.*, vol. 68, no. 11, pp. 10651-10662, Nov. 2019.
- [12] W. Wen, and L.-T. Hsu, "3D LiDAR Aided GNSS NLOS Mitigation in Urban Canyons," *IEEE Trans. Intell. Transp. Syst.*, pp. 1-13, Oct. 2022.
- [13] W. Wen, G. Zhang, and L.-T. Hsu, "Correcting NLOS by 3D LiDAR and building height to improve GNSS single point positioning," *NAVIGATION*, vol. 66, no. 4, pp. 705-718, Dec. 2019.
- [14] L. Benvenuto, T. Cocco, and G. Delzanno, "An Adaptive Algorithm for Multipath Mitigation in GNSS Positioning with Android Smartphones," *Sensors*, vol. 22, no. 15, pp. 5790, Aug. 2022.
- [15] H. Zhou, Z. Li, C. Liu, J. Xu, S. Li, and K. Zhou, "Assessment of the performance of carrier-phase and Doppler smoothing code for low-cost GNSS receiver positioning," *Results Phys.*, vol. 19, Dec. 2020.
- [16] H.-F. Ng, G. Zhang, K.-Y. Yang, S.-X. Yang, and L.-T. Hsu, "Improved weighting scheme using consumer-

- level GNSS L5/E5a/B2a pseudorange measurements in the urban area," *Adv. Space Res.*, vol. 66, no. 7, pp. 1647-1658, Oct. 2020.
- [17] G. Shinghal, and S. Bisnath, "Conditioning and PPP processing of smartphone GNSS measurements in realistic environments," *Satell. Navig.*, vol. 2, no. 1, pp. 10, Apr. 2021.
- [18] C. Shi, S. Guo, L. Fan, S. Gu, X. Fang, L. Zhou, T. Zhang, Z. Li, M. Li, W. Li, C. Wang, and Y. Lou, "GSTAR: an innovative software platform for processing space geodetic data at the observation level," *Satell. Navig.*, vol. 4, no. 1, pp. 18, Jul. 2023.
- [19] S. Gu, C. Gan, C. He, H. Lyu, M. Hernandez-Pajares, Y. Lou, J. Geng, and Q. Zhao, "Quasi-4-dimension ionospheric modeling and its application in PPP," *Satell. Navig.*, vol. 3, no. 1, pp. 24, Nov. 2022.
- [20] J.-C. Juang, and Y.-H. Chen, "Accounting for data intermittency in a software gnss receiver," *IEEE Trans. Consum. Electron.*, vol. 55, no. 2, pp. 327-333, May. 2009.
- [21] Z. Yao, M. Lu, and Z. Feng, "Spreading code phase measurement technique for snapshot GNSS receiver," *IEEE Trans. Consum. Electron.*, vol. 56, no. 3, pp. 1275-1282, Aug. 2010.
- [22] J. Wang, F. Zheng, Y. Hu, D. Zhang, and C. Shi, "Instantaneous Sub-meter Level Precise Point Positioning of Low-Cost Smartphones," *NAVIGATION: Journal of the Institute of Navigation*, vol. 70, no. 4, May. 2023.
- [23] S. Gu, C. Dai, W. Fang, F. Zheng, Y. Wang, Q. Zhang, Y. Lou, and X. Niu, "Multi-GNSS PPP/INS tightly coupled integration with atmospheric augmentation and its application in urban vehicle navigation," *J. Geod.*, vol. 95, no. 6, pp. 64, May. 2021.
- [24] J. Wang, C. Shi, M. Xia, F. Zheng, T. Li, Y. Shan, G. Jing, W. Chen, and T. C. Hsia, "Seamless Indoor-Outdoor Foot-Mounted Inertial Pedestrian Positioning System Enhanced by Smartphone PPP/3-D Map/Barometer," *IEEE Internet Things J.*, vol. 11, no. 7, pp. 13051-13069, Apr. 2024.
- [25] M. Adjrad, and P. D. Groves, "Intelligent Urban Positioning: Integration of Shadow Matching with 3D-Mapping-Aided GNSS Ranging," *J. Navig.*, vol. 71, no. 1, pp. 1-20, Aug. 2017.
- [26] J. Paziewski, R. Sieradzki, and R. Baryla, "Signal characterization and assessment of code GNSS positioning with low-power consumption smartphones," *GPS Solutions*, vol. 23, no. 4, pp. 98, Jul. 2019.
- [27] L. Dai, Z. Wang, J. Wang, and Z. Yang, "Positioning with OFDM signals for the next- generation GNSS," *IEEE Trans. Consum. Electron.*, vol. 56, no. 2, pp. 374-379, May. 2010.
- [28] X. Mao, D. Arnold, V. Girardin, A. Villiger, and A. Jäggi, "Dynamic GPS-based LEO orbit determination with 1 cm precision using the Bernese GNSS Software," *Adv. Space Res.*, vol. 67, no. 2, pp. 788-805, Jan. 2021.
- [29] I. Kashani, P. Wielgosz, and D. A. Grejner-Brzezinska, "On the reliability of the VCV Matrix: A case study based on GAMIT and Bernese GPS Software," *GPS Solutions*, vol. 8, no. 4, pp. 193-199, Dec. 2004.
- [30] J. Wang, F. Zheng, C. Shi, Y. Hu, Y. Xue, Q. Li, and W. Chao, "Fast Convergence Algorithm of Precise Point Positioning Towards Smartphones and its Application in the Urban Environment," *Proceedings of the 35th International Technical Meeting of the Satellite Division of The Institute of Navigation (ION GNSS+ 2022)*, pp. 3031-3044, Sep. 2022.
- [31] J. Wang, C. Shi, F. Zheng, C. Yang, X. Liu, S. Liu, M. Xia, G. Jing, T. Li, W. Chen, Q. Li, Y. Hu, Y. Tian, and Y. Shan, "Multi-frequency smartphone positioning performance evaluation: insights into A-GNSS PPP-B2b services and beyond," *Satell. Navig.*, vol. 5, no. 1, pp. 25, Aug. 2024.
- [32] A. Rustamov, A. Minetto, and F. Dovis, "Improving GNSS Spoofing Awareness in Smartphones via Statistical Processing of Raw Measurements," *IEEE Open J. Commun. Soc.*, vol. 4, pp. 873-891, Mar. 2023.